

# Numerical lamb wave modeling and analysis for cure cycle shortening of carbon fiber composites

Journal of Composite Materials  
2023, Vol. 57(9) 1683–1703  
© The Author(s) 2023  
Article reuse guidelines:  
[sagepub.com/journals-permissions](https://sagepub.com/journals-permissions)  
DOI: 10.1177/00219983231160874  
[journals.sagepub.com/home/jcm](https://journals.sagepub.com/home/jcm)  


Elie Mahfoud  and Mohammad Harb

## Abstract

Advanced carbon fiber composites are renowned for their great tenacity as, although being thin, they provide great strength, keeping structures light in weight. The composites industry struggles with longer cure times when compared to other traditional material production. In this study, a computational model for a carbon fiber reinforced polymers (CFRP) plate is developed to imitate experimental monitoring of its cure cycle and degree of cure. The CFRP storage modulus is measured during the curing cycle with the aid of dynamic mechanical analysis, and its trend is incorporated into COMSOL combined structural and electrostatics multiphysics to replicate the same mechanical fluctuations during oven curing. Then, Lamb waves are excited and sensed via sandwiched piezoelectric transducers in a reusable Polytetrafluoroethylene sensing film to monitor the structural health of the structure. Minimum viscosity, gelation and vitrification are cure parameters observed from analyzing voltage and velocity curves of the  $A_0$  mode of the sensed signal. The cure cycle is trimmed, and the same cure parameters are shown offset by the  $l$  h deducted, proving that the numerical model is valid. Further analysis of the numerical voltage and velocity curves suggests an additional cure parameter defined as “gelation initiation” when compared directly to the experimental trends. Additionally, the decomposition of different wavefield modes is scrutinized to describe their scattering throughout the layered structure. Results show a new entrapped antisymmetric mode appearing inside the CFRP laminate at the start of the cure, which suggests that the previously studied  $A_0$  mode had been initially converted from the CFRP  $S_0$  mode.

## Keywords

Carbon fiber composites, cure cycle monitoring, cure kinetics, Lamb waves, wave propagation, numerical modeling, non-destructive testing, gelation, vitrification

## Introduction and background

Although carbon fiber reinforced polymers (CFRPs) have been used in many applications such as vehicles structures, wind turbine rotor blades, basic construction, and many sports and musical equipment, there are still many industries that these composites can infiltrate into with enough research.<sup>1</sup> However, the main problems with the composites industry that limit the fabrication are the long curing cycles and post-cure processing and finishing requirements when compared to traditional metal materials.<sup>2</sup> These curing cycles are often provided by the manufacturers with an unwanted large safety factor that if reduced, can lead to faster manufacturing of CFRPs which innately makes them more popular with many industries.<sup>3</sup> Hence, the need for advanced methods to monitor and evaluate the curing process of carbon fiber composites is growing. In our previous work, we designed and implemented a reusable

system that successfully monitored in-lab composite structures during curing using ultrasonic waves.<sup>4</sup> Then, the same system was used for effectively reducing the cure cycle time of a weaved CFRP without affecting its mechanical and thermal properties when fully cured.<sup>5</sup> In this work, we create a finite element computational model that, when paired with small scale experimental dynamic mechanical analysis, monitors the curing cycle of CFRP structures through guided Lamb waves.

---

Laboratory of Smart Structures and Structural Integrity, Department of Mechanical Engineering, American University of Beirut, Beirut, Lebanon

### Corresponding author:

Elie Mahfoud, Department of Mechanical Engineering, American University of Beirut, Riad El Solh, Beirut 1107 2020, Lebanon.  
Email: [enm08@mail.aub.edu](mailto:enm08@mail.aub.edu)

Cure monitoring is any established process during which a designated material property is measured to evaluate the degree of cure. Typical monitoring techniques for resin curing consist of dynamic mechanical analysis (DMA), thermogravimetric analysis (TGA), differential scanning calorimetry (DSC), rheological analysis, emergent dielectric analysis (DEA), etc.<sup>6</sup> These in-lab methods provide crucial information about the cure of thermosetting polymers such as glass transition temperature ( $T_g$ ), resin viscosity flow, formation of gel and overall crosslinking, resulting in degree of cure monitoring.<sup>7</sup> Braun et al. analyzed molecular processes of an epoxy resin during curing using Fourier transform infrared (FTIR) by DSC and TGA.<sup>8</sup> Sawicz-Kryniger et al. recently compared and evaluated the performances of Fluorescence probe technique (FPT), DSC, and FTIR in real time epoxy cure monitoring.<sup>9</sup> Kister and Dossi established a baseline study for cure monitoring CFRP composites inside a DMA machine in a single cantilever setup.<sup>10</sup> They cured a unidirectional carbon/epoxy at three different frequencies and labelled several curing parameters including matrix softening, gelation, vitrification, and solidification of the composite. On the other hand, Bilyeu et al. combined DSC and DMA to construct the time temperature transformation diagram for an epoxy glass FRP.<sup>11</sup> The three-point bending setup enabled them to find vitrification peak more clearly in the tan delta graph compared to the storage modulus. Moghaddam et al. designed and embedded microscale interdigital capacitive sensors within glass FRP composites to monitor its curing.<sup>12</sup> These small size sensors barely affect the mechanical performance of the final cured product while maintaining good DEA readings throughout the curing process due to their flexibility and high temperature resistance. With the exception of the different DEA techniques, the mentioned methods are usually limited to setups within labs or are applicable only on small scales. Industrial production require more feasible methods to monitor their processing on larger scales. Thus, in recent years, several polymer cure monitoring methods that can also be applied in industry emerged because of their feasibility. Roberts and Davidson used fibre optical sensors to measure electrical resistance measurements and dielectric impedance changes during curing.<sup>13</sup> Ultrasonic measurements by transmitting and receiving elastic waves were also studied to read sensitive information about the material changes during the curing process.<sup>14</sup> Several studies involved bulk waves to characterize the resin curing on its own since these waves can be correlated directly to the evolving modulus and density of the material.<sup>15</sup> Longitudinal and shear moduli are directly proportional to the density and the square of longitudinal and shear wave velocities, respectively. Then, one can also calculate the Young's modulus and Poisson's ratio by simple linear equations relating the latter two properties to the longitudinal and shear moduli.<sup>16</sup> This is why these

waves are of interest, since the reading of their velocities and attenuation gives knowledge about material stiffness and viscosity, respectively. The evolution of these mechanical properties during curing thus offers good estimation of the degree of cure.<sup>17,18</sup> This simple correlation only applies in isotropic material like pure resins and metals, whereas in complex orthotropic material like the studied CFRP composites, more multifaceted waves are needed. Pavlopoulou et al. used an empirical mode decomposition to successfully monitor the cure level of a laminated composite after transmitting guided Lamb waves through the plate.<sup>19</sup> Lionetto and Maffezzoli<sup>20</sup> and Hudson and Yuan<sup>21</sup> determined the onsets of gelation and vitrification of composites cure using Lamb waves. The former study used air-coupled transducers while the latter relied on contact piezoelectric ceramic transducers (PZTs) and analyzed the antisymmetric  $A_0$  mode. These cure onsets are essential parameters in determining the curing phase.

Numerical modeling was adopted long before the emergence of user-friendly commercial finite element softwares to optimize the experimental costs both in research and industry before manufacturing. Computational studies of polymer cure monitoring can be divided into two main categories. The first is examining the chemical reactions that are initiated by heat, affecting the degree of cure, and studies the cycles for more optimized cure.<sup>22</sup> The second category focuses on developing predictive viscoelastic models that use experimental validation to forecast the changes in mechanical behavior during resin or polymer composites curing.<sup>23</sup> Anandan et al. used COMSOL Multiphysics to characterize a cure cycle for a CFRP composite.<sup>24</sup> They obtained cure constants through DSC experiments and combined a chemical cure kinetics module with heat transfer module in the software to change the second soaking stage into a minor ramp with a different initial temperature. Garschke et al. also studied the curing kinetics parameters by DSC and exported the results to a developed model that simulates the heat diffusion of the cure cycle.<sup>25</sup> Their model was also used to predict viscosity. Behzad and Sain also used COMSOL to simulate the curing process of a natural fiber composite and predict the temperature profile by validating experimentally.<sup>26</sup> Then, they used the same model for predicting the cure of a more complex three-dimensional automotive mirror casing part. On the other hand, Dai et al. used the same two modules in COMSOL with an added mechanics module which enables the use of viscoelasticity.<sup>27</sup> By doing so, they predicted the residual stresses for a composite plate during curing and compared the results to a modified viscoelastic CHILE model. Zheng and Zhang decomposed the use of viscoelasticity within COMSOL by manually adding a structural relaxation study to the available Williams-Landel Ferry (WLF) stress relaxation shift function.<sup>28</sup> Patham also compared his cure-time-temperature superposition

viscoelastic model in the same software to a regular elastic model to see the differences in stress residuals on constrained resin during curing.<sup>29</sup> Yoo et al. was one of the rare studies that implemented experimental DMA storage modulus results into a finite element method (FEM) software to compare the cure parameters onsets numerically and experimentally.<sup>30</sup> They implemented the storage modulus curves of DMA curing into ABAQUS and measured the strains using dielectrometry sensors. They identified the liquid, rubbery, and solid phases along with gelation and vitrification points in both numerical and experimental studies. Then, they used their validated computational model to simulate the curing of a wheel rim made of the same CFRP composites. To our knowledge, no studies were found to apply this principle of importing modulus changes into an FEM software to simulate the curing of composites via guided Lamb waves. Similar to the latter study, our work does not take into consideration the curing kinetics nor the viscoelastic response of the cured material since that would add much more physics modules resulting in too many degrees of freedom and extensive simulation time. Also, the chemical cure kinetics and the viscoelastic modules require DSC and stress relaxation experiments, respectively, to find certain parameters and constants, which would make this study unrealistically broad.

Reducing the manufacturing time is crucial to the composites industry as it would reduce costs and increase production.<sup>31</sup> This is why it is essential to try shortening the curing cycle of the used CFRP while maintaining its mechanical and thermal performance. The cure cycle trimming may even optimize the crosslinking process and reduce the deterioration of cure as most manufacturers provide cycles that have high safety factors which makes for unoptimized final cured product.<sup>32</sup> The focus of this paper is to computationally monitor the curing of a CFRP plate using Lamb waves while having the cure cycle shortened. Lamb waves are transmitted and read by PZTs sandwiched between two skived Polytetrafluoroethylene (PTFE) layers. This flexible sensing system adheres temporarily to the CFRP prepreg during curing and can be reused, thus also reducing consumables waste and expediting the setup in subsequent experiments. PTFE, commercially known as Teflon, is usually used as artificial delamination between the composite laminas.<sup>33</sup> It is the optimum material for enclosing the PZTs because of its chemical inertness and high temperature withstanding. Also, its acoustic impedance is similar to that of epoxy resins, which is ideal for wave propagation considerations.

This paper first introduces the fundamentals of guided Lamb waves and shows the experimental setup and analysis of ultrasonic cure monitoring and cycle shortening of a woven CFRP composite. Then, the DMA curing results of the same composite are shown through storage modulus ( $E'$ ) curves at different frequencies. These curves are extracted

and implemented into COMSOL Multiphysics FEM software for both the original and the shortened curing cycles. Two modules are used to create the piezoelectricity effect in the software. After optimizing the model for both solver and mesh size, the parametric sweep results are shown in form of signal comparison for both cycles to their experimental counterparts. Also, the numerical velocity and amplitude curves are extracted for each cycle. Finally, the viability of this computational method is discussed by comparing numerical and experimental results and showing the advantages and limitations of this study.

## Experimental testing

### Fundamentals of lamb waves

In the early 20<sup>th</sup> century, Horace Lamb demonstrated that elastic waves, existing in infinitely-long thin solid media, reflect on the upper and lower boundaries to propagate and separate into two groups of wave modes: symmetrical (S) and anti-symmetrical (A).<sup>34</sup> These waves are now termed after his name and have complex properties depending on many factors including plate thickness, excitation frequency, wavelength, etc.<sup>35</sup> Although both symmetric and anti-symmetric Lamb wave modes are constituted of mixed longitudinal and shear vibrations, the former can be simplified by a longitudinal wave motion whereas the latter can be approximated as a bending wave. Their propagation characteristics vary with the excitation type, angle, and the structure shape itself. The following equations describe the motion of Lamb waves inside a linear elastic isotropic thin plate that is unbound in the x and y directions:

$$\frac{\omega^4}{C_T^4} = 4k^2 q^2 \left[ 1 - \frac{p \tan\left(\frac{ph}{2} + \gamma\right)}{q \tan\left(\frac{qh}{2} + \gamma\right)} \right]; \quad (1)$$

$$p^2 = \frac{\omega^2}{C_L^2} - k^2; \quad (2)$$

$$q^2 = \frac{\omega^2}{C_T^2} - k^2; \quad (3)$$

where  $\gamma$  represents the S and A wave modes for values of 0 and  $\pi/2$  respectively,  $h$  is the plate's finite thickness,  $k$  is the wave number,  $\omega$  is the angular frequency,  $C_L$  and  $C_T$  are respectively the longitudinal and transverse velocities of the bulk material.

Since Lamb waves are theoretically present in semi-infinite plates, "guided Lamb waves" is a more practical term to identify Lamb-like waves that are excited in finite thin plates and cylindrical structures.<sup>36</sup> Guided waves have been used in many non-destructive testing (NDT) applications to assess the structural health of metallic and non-

metallic structures. After excitation, they propagate rather predictably and have high sensitivity to any type of damage. Easy data collection, material properties prediction, and precise damage localization are some of the reasons that made these waves a reliable substitute to traditional NDT tools.<sup>37</sup> For example, Harb and Yuan identified delamination and assessed impact damages in composite CFRP laminates using a fully non-contact system made of air-coupled transducers which transmit and receive a basic antisymmetric  $A_0$  Lamb wave mode.<sup>38</sup> Fakhri et al. studied the plastic deformation influence in friction stir welded aluminum plates joint on the propagation behavior of guided Lamb waves to assess any discontinuity in the material within the weld region.<sup>39</sup>

One major characteristic of Lamb waves is their dispersion: the velocity of each propagating mode is not constant but dependant on the excited frequency. For a woven 1 mm – thick CFRP plate, a frequency range between 50 kHz and 300 kHz abridges the propagating sets of Lamb waves to only the first symmetric and asymmetric modes:  $S_0$  and  $A_0$ , yielding simpler signal processing and mode identification. Typical dispersion curves show that  $S_0$  is faster than  $A_0$  at these low ultrasonic frequencies. As the frequency increases drastically, both modes converge into a steady speed that is identified as a Rayleigh-Lamb wave velocity, which is close to the speed of sound of the material.<sup>40</sup> Also, these modes propagate with different displacement amplitudes that also vary versus frequency, making one of the modes more dominant over the other depending on each excited frequency, regardless of their speed. Figure 1 shows the experimental (a) tuning and (b) dispersion curves of a fully cured woven CFRP laminate consisting of 3 layers of out-of-autoclave XPREG XC110 woven prepreg [0/90/0] and that has a final thickness of 1 mm. The tested frequency range is between 10 and 400 kHz. In Figure 1(b), the group velocity of  $S_0$  fluctuates between 5500 and 6500 m/s whereas the  $A_0$  velocity ascends from 600 to almost 1300 m/s before its amplitude drastically diminishes and the mode disappears at 150 kHz.

In Figure 1(a),  $A_0$  is clearly dominant up to a frequency of 100 kHz where  $S_0$  becomes prevalent after that. The symmetric mode has an amplitude peak at 330 kHz whereas the voltage peak for  $A_0$  occurs at 70 kHz. The latter frequency is chosen to excite the CFRP laminate during the cure monitoring experiment due to many factors. First,  $A_0$  is at its highest respective strain compared to  $S_0$ , so not only is  $A_0$  dominant at this frequency, but the highest difference between the two voltage curves occurs at this point. The decision to work with  $A_0$  also derives from the fact that the anti-symmetric mode propagates in an out-of-plane manner along the moving path, thus it is more suitable for the propagation through the thin PTFE film and into the CFRP composite and the aluminum tooling plate. Whereas the  $S_0$  mode, propagating in-plane, severely attenuates when moving from one material boundary to another in the z-direction.

### Cure monitoring

To monitor the cure of the discussed CFRP prepreg, a vacuum bagging setup inside the oven shown in Figure 2 is attached to a real time monitoring system. Two disc-like PZT-5J transducers (0.5 mm thick, 7 mm diameter, 320°C Curie temperature) are sandwiched by 0.25 mm thick Skived PTFE layers. This sensing film is in direct contact above the CFRP laminate. During vacuum, it adheres temporarily to the laminate, and debonds easily after full curing. This brief adhesion yields enough wave propagation to go through inside both the laminate and the tooling plate. The latter is sprayed with a silicone release agent so that the CFRP does not glue to it. This creates a PTFE-CFRP-Aluminum path for the signal to go through while the cure process occurs. The CFRP laminate and the PTFE films are  $220 \times 350 \text{ mm}^2$  in width and length, respectively. The distance between the PZTs inside the PTFE is 240 mm along the  $0^\circ$  direction of the fibers and centered along the  $90^\circ$  direction. The curing cycle set by the manufacturer is as follows: temperature ramps up from room to 70°C in

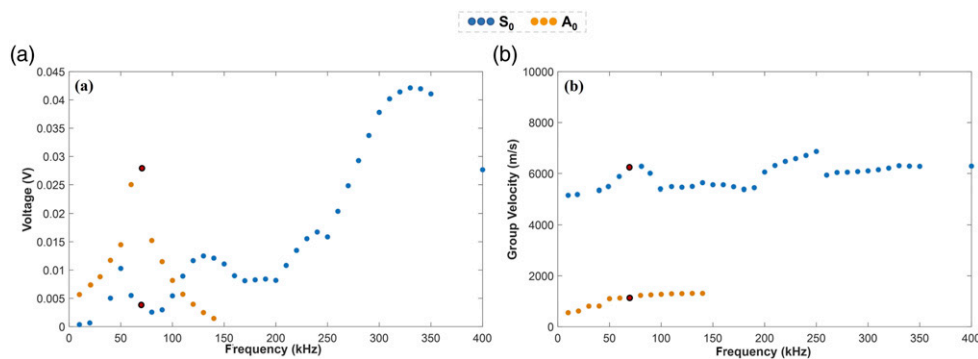


**Figure 1.** (a) Tuning curves showing voltage amplitude of each mode versus frequency, and (b) dispersion curves showing group velocity of each mode versus frequency, both for the cured 1 mm-thick woven CFRP plate.

50 min, the part soaks at this temperature for 4 h, temperature ramps up again to 120°C within 25 min, the part soaks for 1 h, and then cools naturally.

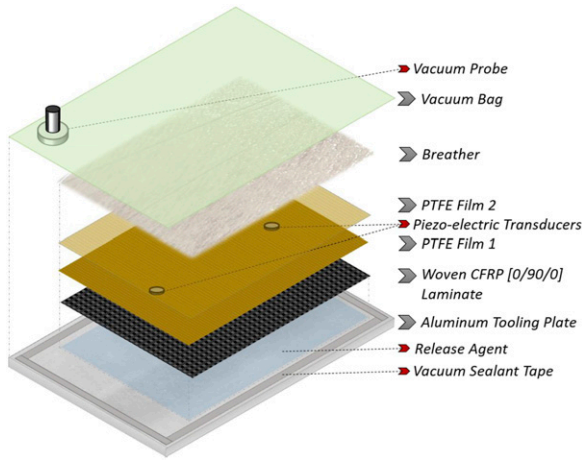


**Figure 2.** Layup process of the CFRP composite along with the described sensing film layers.

The described sensing film is connected, from the wired and soldered PZT actuator to the amplifier which intensifies the five-peak sinusoidal Hanning-windowed signal generated by the wave generator. The PZT sensor is connected to an oscilloscope that records the travelling wave signal every 10 min. The cure cycle shortening is done by cutting 1 h from the first soak period of the cycle because minimum viscosity always occurs at the end of this long soak and the other cure parameters are present after that. Thus, the total time of the 3 h-soak cure cycle is 390 min compared to 450 min for the original 4 h-soak cycle. The monitoring experiment is repeated for the new cycle and data for both cycles are analyzed through the speed and amplitude of the recorded  $A_0$  mode. Aggelis and Paipetis showed that velocity is linked directly to the stiffness of the resin, while viscosity relates to the attenuation of the propagating wave.<sup>17</sup> Thus, each one of these two studied wave parameters gives better indication about some cure parameters, when compared to the other. Vitrification is more effectively extracted from the velocity curves while the minimum viscosity and gelation points are better determined from the voltage curves.<sup>20</sup> Figure 3(a) and (b) show

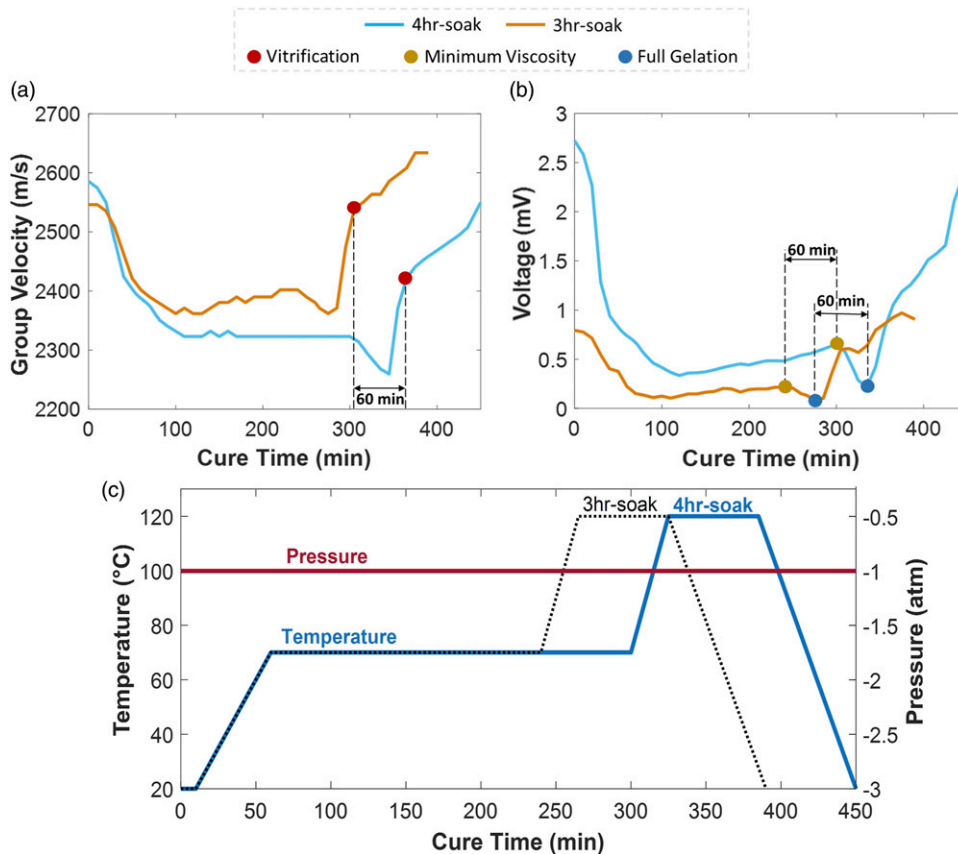


**Figure 3.** (a) Group velocity and (b) voltage amplitude of the recorded  $A_0$  mode from the experimentally tested CFRP laminates for both curing cycles versus cure time.<sup>4</sup> (c) Shows the cure cycle proposed by the manufacturer (4 hr-soak) and the shortened cycle (3 hr-soak), during which the composite is put under vacuum pressure in an out-of-autoclave setup.

the group velocity and voltage curves, respectively, for both 4 h-soak and 3 h-soak experiments. In Figure 3(b), minimum viscosity of the composite appears at the maximum before the start of the second ramp. At the following minimum, for both cycles, full gelation occurs denoting the presence of rubber in the polymer. During the following ascent but in Figure 3(a), the change of slope denotes the vitrification point. Comparing the two cycles together, all three cure parameters are clearly shifted 60 min backward in the 3 h-soak curves. Hence, this cycle time shortening does not affect curing from an ultrasonic standpoint. Figure 3(c) shows both the original curing cycle (4 h-soak) and the 3 h-soak shortened cycle versus cure time along with the vacuum pressure applied during the process. It is of interest to note that the temperature variation effects on the Lamb wave signal are previously studied<sup>4</sup> and the thermal effect on the aluminum tooling plate shows that although the voltage and velocity passing through the sole aluminum are affected by the heat ramps proportionally, they do not change the three discussed cure points shown in Figure 3.

### Dynamic mechanical analysis

To ensure that the cure cycle reduction did not affect the mechanical performance of the fully cured CFRP by the shortened cycle, DMA is used to compare mechanical and thermal properties of the two curing cycles. The  $T_g$  and creep testing results show that the properties of the 3 hr-soak cured specimens are slightly better than those of the 4 hr-soak specimens. The formers have a higher storage modulus, higher  $T_g$  (both onset and  $T_c$ ), and even better fatigue properties.<sup>5</sup> After proving the feasibility of the cycle shortening by DMA and tensile testing from that previous study, DMA can also be used to monitor the change in storage modulus during curing for both cycles. The trend of this change will be extracted and implemented into the computational model. Figure 4 shows the storage modulus ( $E'$ ) versus the cure time for the 4 hr-soak cure cycle inside the DMA at four different frequencies. Each frequency test is repeated at least five times and the curves shown are averaged for each respective frequency. The averaged curve of all frequencies is also shown in the figure. Curing is performed using  $30 \times 10 \times 1 \text{ mm}^3$  woven CFRP specimens of the same orientation as the cure monitoring experiments, while implementing the same cycle ramps and soaks in a single cantilever setup and recording data every second.

Higher and lower frequencies are not available to test at the selected applied force of 2 N. Notice that if the 5 Hz curve is neglected, the three other frequencies have a trend such that the higher the frequency, the steeper the curve goes downward in the liquid and rubbery states, and the higher it reaches in the glassy state. However, the 5 Hz curve lies between the 0.5 Hz and the 1 Hz curves for most of the curing cycle, and below the 0.5 Hz curve after vitrification.

Nonetheless, it follows the same curve trend and yields the same cure parameters. On the zoomed-in part of Figure 4, the minimum viscosity point varies only 3 min between 299 min for the 1 Hz and 10 Hz curves and 302 min for the 0.5 Hz curve. The full gelation point varies 5 min between 314 min and 319 min. On the other hand, the vitrification point is almost constant between 330 min for the 0.5 Hz and 5 Hz curves and 331 min for the 1 Hz and 10 Hz curves. This shows that these variations, although present, are minimal and do not affect the average storage curve considerably. This is why testing the 3 hr-soak cycle and comparing its average  $E'$  curve to the shown 4 hr-soak average curve is a valid approach as the frequency variation is not respectively significant. Note that the gelation and vitrification points occur at previous times when compared with Lamb wave results from Figure 3: gelation is at 315 min in the DMA results compared to 335 min in the ultrasonics testing, whereas vitrification is at 330 min compared to 365 min (Figures 3 and 4, respectively). Also, the final storage modulus in the average  $E'$  curve reaches around 5 GPa, where in reality, tensile testing of cured samples shows that the Young's modulus in the  $0^\circ$  direction is averaged at 51 and 56 GPa for the 4 hr- and 3 hr-soak cycles, respectively. These two setbacks could be due to differences in curing environment as there is no vacuum present in the DMA chamber. The small specimen size affects the heat transfer process compared to the large CFRP plate along with all the added bagging consumables and aluminum tooling plate in the ultrasonic cure testing. Also, the cyclic loading and constant straining of the DMA specimens might deteriorate the final mechanical properties and affect the cure parameters. However, this is not a major concern as these DMA curves are only compared to their ultrasonic testing counterparts qualitatively.<sup>41</sup>

Figure 5 shows the extracted DMA curing results of the averaged  $E'$  curves for both 4 hr-soak and 3 hr-soak cycles after amplifying the ascent in the rubbery and glassy regions by a multiple of four. This is done to make the final modulus of both curves higher and more impactful in wave characterization within the numerical model in COMSOL. Note that the modulus reaches higher values for the 3 hr-soak cycle in the figure as expected and previously concluded from tensile and DMA testing results.<sup>5</sup>  $E'$  reaches between 20 to 30 GPa in these curves but in reality, cooling inside the DMA is proceeded for another 5 hours and the storage modulus, after the same amplification, reaches 45 GPa for the 4 hr-soak which is 88% of its real final Young's modulus, and 52 GPa for the 3 hr-soak which is 93% of its cured Young's modulus. Hence, this multiplication for the curves gives a truer representation for mechanical properties inside the cure monitored CFRP specimens than the actual DMA curing storage curves. The importance lies in the qualitative nature of the curve trends imported to the FEM software, compared to the quantitative actual storage moduli data.

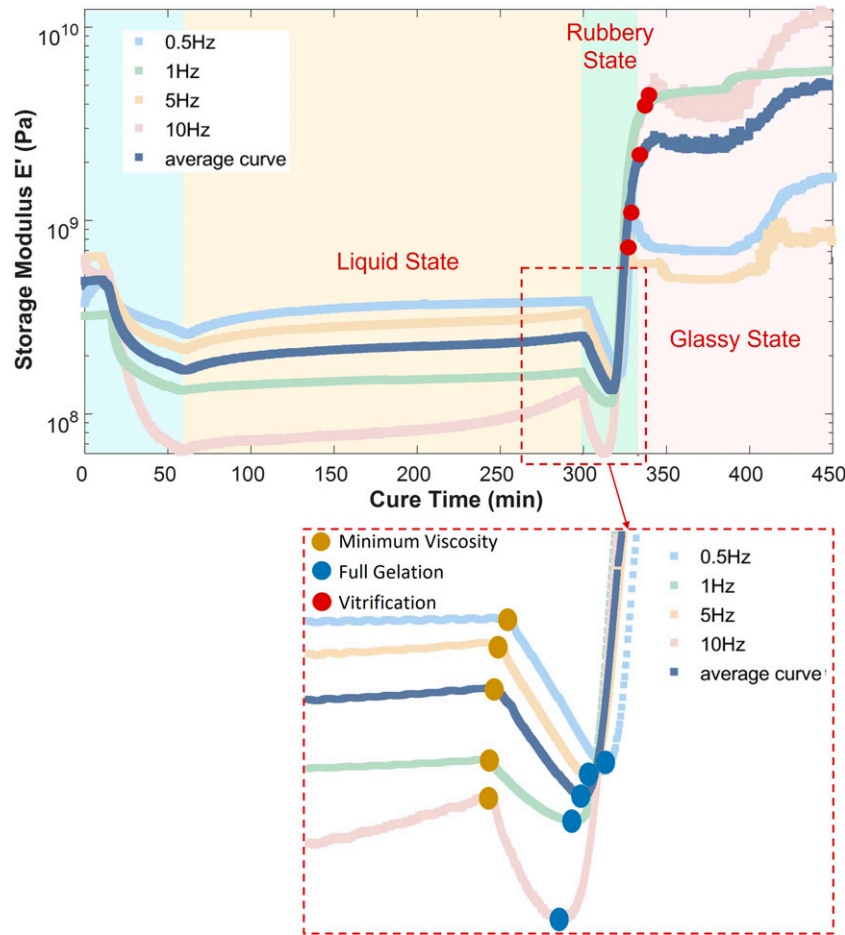


**Figure 4.** DMA 4 hr-soak curing results for the woven CFRP specimens tested with the shown frequencies.

## Computational modeling

### Material properties

In COMSOL Multiphysics FEM software, three different blank materials are defined, and one PZT-5J material is assigned from the software's library for the two transducers. Aluminum-1050 and Skived PTFE are defined as isotropic material so that the solid mechanics module requires only each of their Young's modulus ( $E$ ), Poisson's ratio ( $\nu$ ), and density ( $\rho$ ), while the additional electrostatics module requires only the relative permittivity ( $\epsilon_r$ ). The material properties for aluminum are found from literature whereas the properties for PTFE are obtained from the manufacturer's technical sheets. Properties for both of these materials are shown in Table 1 and are assumed to stay constant during the curing cycle. These mechanical properties would be affected by the elevated temperatures, but since it is validated that this thermal effect on the PTFE and tooling plate does not affect the cure monitoring of the laminates by keeping the voltage and velocity curves' slope changes

intact,<sup>7</sup> and for the scope of this study, these properties are considered stable throughout the cure.

The woven CFRP laminate is considered an orthotropic material that has the final cured mechanical properties shown in Table 2 for both cycles. The Young's modulus in the first direction ( $E_1$ ) is known from previous tensile testing on specimens cured in each cycle.<sup>5</sup> The modulus in the planar  $90^\circ$  direction ( $E_2$ ) is considered the same as  $E_1$  since this is a woven composite. The modulus in the out-of-plane direction ( $E_3$ ) is taken as 10% from  $E_1$  and  $E_2$  since it is also assumed to be close to the modulus of epoxy. The remaining shear moduli and Poisson's ratios in all directions are obtained from literature by having these properties proportional to  $E_1$  and  $E_2$ . To make the analysis simpler, Poisson's ratios are assumed the same for both cycles since not enough information is found about the relationship between them and the moduli. The fully cured density is calculated in-lab and the relative permittivity is found from literature.<sup>42</sup> The latter is assumed constant throughout the curing cycle. The moduli and Poisson's

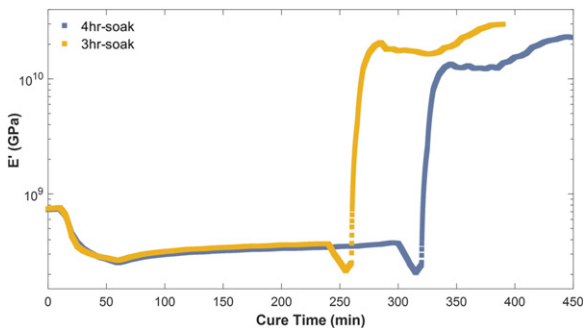


**Figure 5.** The amplified DMA storage modulus average curves for both cycles that are implemented into the computational model.

**Table 1.** The required properties in COMSOL for the present isotropic materials.

	E (GPa)	$\nu$	$\rho$ (kg/m <sup>3</sup> )	$\epsilon_r$
Aluminum-1050	70	0.33	2700	1
Skived PTFE	0.55	0.46	2200	2.1

ratios shown in the table are for the fully cured state in each cycle. To implement the changes in these mechanical properties during curing in COMSOL, a parametric study is deployed on these variables where their values are stored for each 5 minutes of the curing cycle. This is done by segmenting the previous DMA  $E'$  average curves from Figure 5. Then,  $E_1$  and  $E_2$  for each cycle are considered to have the same values as the averaged  $E'$  moduli throughout the cycle. Figure 6(a) shows the values of  $E_1$  and  $E_2$  implemented into COMSOL for the 4 hr-soak cycle. The remaining moduli  $E_3$ ,  $G_{12}$ ,  $G_{23}$ , and  $G_{13}$  have the same cure curve trend as Figure 6(a) but the values are proportional to their final cured state from Table 2. For example, the curve for the implemented  $E_3$  modulus for the 4 hr-soak cycle is the same as in Figure 6(a) curve but divided by 10.

As for the Poisson's ratios  $\nu_{12}$ ,  $\nu_{23}$ , and  $\nu_{13}$ , the proportionality is applied with regards to the fully cured values in Table 2. However, their trends do not follow the same averaged DMA storage curve since during the consolidation of the epoxy resin in the first soak period, Poisson's ratio is usually elevated near an incompressible fluid value of 0.5 instead of having a decrease. The rubbery and glassy regions in the curve trends are adjusted to fulfill several claims about the Poisson's ratio during curing for an epoxy resin since  $\nu_{23}$  and  $\nu_{13}$  are mainly very similar to the isotropic Poisson's ratio of the impregnated epoxy within the composite. According to Saseedran et al., experimental evidence shows that the viscoelastic Poisson's ratio in the rubbery region can be assumed approximately 0.5 for epoxy resins.<sup>43</sup> Obrien

et al. states that the Poisson's ratio reaches equilibrium where  $\nu = 0.4925$  when the shear relaxation modulus fall below a certain value.<sup>44</sup> Since in the scope of this study, viscoelasticity is not considered for the main studied model, linear elastic Poisson's ratios are considered for  $\nu_{23}$  and  $\nu_{13}$  to be just below 0.5 at full gelation and decaying logarithmically until reaching a value slightly higher than that of the fully cured composite.<sup>45,46</sup> The final trend implemented in COMSOL for these two Poisson's ratios for the 4 hr-soak cycle is shown in Figure 6(b). The  $\nu_{12}$  trend is the same but proportional to its final fully cured value of 0.05. Due to the chemical shrinkage rise from 0 to almost 6% after full curing,<sup>47</sup> and the expansion of epoxy due to the heat cure cycle, the density of the curing CFRP is estimated to have a maximum change of 5.8%. It is measured in-lab before the start and after the end of curing, and its curing trend seen in Figure 6(c) is based on several statements from literature such as the density of a curing epoxy being maximum at partially cured state.<sup>48</sup> It is also based on the combination of the thermal expansion effect and the chemical shrinkage versus degree of cure curve trend. Thus, the density here slightly increases at the start of the cycle, knowing that the thermal expansion would lead to a decrease, but this latter effect is considered minor when compared to the actual chemical reaction. It rises again during the second heating phase until reaching a maximum during the rubbery phase. After full gelation, it starts heavily decaying before a slope change is noticed just prior to vitrification. After that, it diminishes logarithmically until reaching a final cooled fully cured stage of the CFRP.

### Combined modules and numerical solving

The piezoelectric effect in COMSOL is enabled by combining two physics: structural solid mechanics and electrostatics. The former is governed by the displacement parameters in all three directions whereas the latter is controlled by the voltage calculated from electric displacement field equations. To assign the "Piezoelectric Devices", a Piezoelectric Material tab is inserted for both physics and the two transducers are selected so that the electrical signal can be measured exclusively by their volume. Two Linear Elastic Material tabs are added under solid mechanics. One for the two isotropic materials present and the other for the orthotropic CFRP. Under electrostatics, the upper surface faces of the two PZTs are selected as Ground with zero electric potential, and the lower face of the actuator PZT is designated as the Electric Potential from where the wave is fed and transmitted. The latter is a five-peak sinusoidal Hanning-windowed signal that represents the experimentally actuated wave and is approximated by the following equation:

**Table 2.** Final cured state CFRP mechanical properties for each cycle.

	E1 (GPa)	E2 (GPa)	E3 (GPa)	G12 (GPa)	G23 (GPa)	G13 (GPa)	$\nu/2$	$\nu/3$	$\nu/3$	$\rho$ (kg/m <sup>3</sup> )	$\epsilon_r$
4 hr-soak	51	51	5.1	7.0	4.0	5.0	0.05	0.38	0.38	1800	20
3 hr-soak	56	56	5.6	7.7	4.4	5.5	0.05	0.38	0.38	1800	20

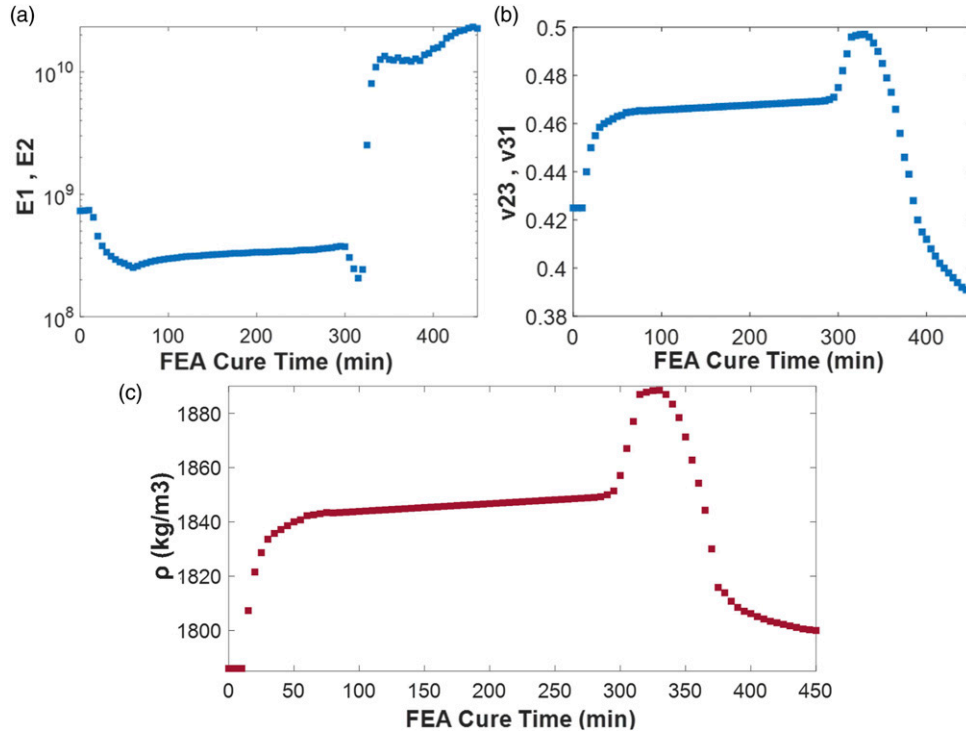


**Figure 6.** Segmented DMA results that are implemented into COMSOL for a parametric study on the mechanical properties of the woven CFRP. (a) Shows  $E_1$  and  $E_2$  for the 4 h-soak cure cycle segmented directly from the averaged  $E'$  curve, (b) shows the  $\nu_{23}$  and  $\nu_{13}$  curves for the 4 hr-soak cycle based on literature and adjusted proportionally for the rubbery and glassy regions from their fully cured value, and (c) shows the density fluctuations during curing based on chemical shrinkage variations.

$$Voltage = C \sin(2\pi f_c t) \left( 1 - \cos\left(2\pi f_c \frac{t}{5}\right) \right) \left( flc2hs(t, .0) - flc2hs\left(\frac{t-5}{f_c}\right) \right); \quad (4)$$

where  $f_c$  is the excited central frequency of 70 kHz,  $t$  is the time in seconds,  $flc2hs$  is a smoothed Heaviside step function with a continuous second derivative without overshoot, and  $C$  is a multiplication factor that one can vary until reaching the desired voltage amplitude. In this case,  $C$  is equal to 41 so that the peak to peak voltage reaches a value of 160 V, mimicking the experimental actuated value. The number of peaks in the Hanning-windowed signal is determined by the number 5 in equation (4), changing this number would change the number of peaks present in the transmitted sinusoidal signal.

The model's geometry is created by building five blocks (three for the laminate) and two cylinders to represent the plates and PZTs, respectively. As shown in Figure 7, the three CFRP laminas lay on top of the aluminum tooling plate. The Skived PTFE film lays above the composite and is grooved to embed two circular PZT transducers that are capable of transmitting mechanical and reading electrical signals along the x-axis. This model is scaled to the actual geometry size of the experimental setup. The vacuum bagging consumables should have little to no effect on the wave propagation, thus they are not included in the model. There is no boundary conditions on the plate, as it is assumed to be floating in void since we are testing for Lamb wave excitation analysis, and fixating a surface would not be ideal for this application.

Figure 8 shows the fully meshed model and a zoomed-in scrutinized area around the actuating PZT. The cylindrical

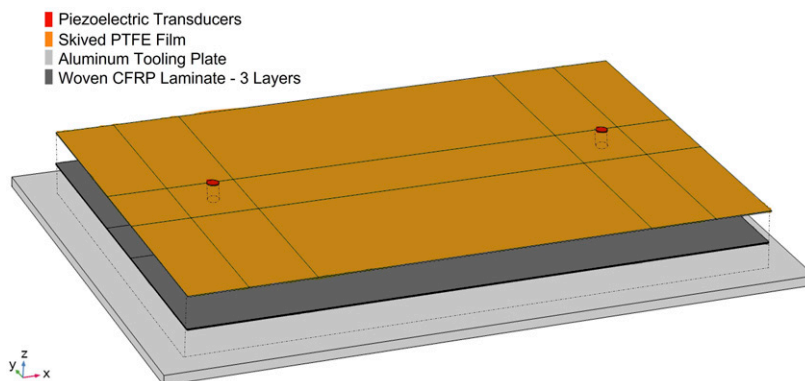


**Figure 7.** Geometry created using the aided design within COMSOL. The parts are spaced from each other in the z-direction only for the purpose of demonstration in this image.

transducers are meshed with free tetrahedral elements since this is an area of interest and the mesh density needs to be relatively high. At some distance from the two PZTs in the x and y-directions, the plates are mapped with quadrilateral or rectangular elements on one surface and extruded throughout the thickness, thus resulting in hexahedral elements for most of the geometry. At the vicinity of the two PZTs, a transition region between the two element types is mapped on its top surface with triangular elements and extruded to result in prism elements. This is done to effectively connect the nodes in-between the hexahedral and tetrahedral elements. As for the sizing, the physics-controlled setting is set to “extremely fine” mesh size, but that still does not give sufficiently small “maximum elements” within the geometry to correctly solve for the wave propagation. When modeling elastic Lamb waves, the mesh density or maximum element size has to be dependent on the phase velocity of the slowest propagating mode, which in this case, is the  $A_0$  mode. Usually, an appropriate maximum element size should not be larger than the tenth of the smallest wavelength.<sup>49</sup> The latter is simply the  $A_0$  mode velocity found from the experimental signals divided by the excited frequency. For this model, the wave travels into many media, especially CFRP and aluminum, which both affect the wave mode separation and speed of the transmission. Thus, mesh size iterations are performed to study the mesh convergence rather than using the previously stated method. Results show that the ratio for wavelength over the maximum element size of 7.75 is sufficient for the first received  $A_0$  mode packet, which is the focus of this study, to converge. The value of the mentioned ratio corresponds to a maximum element size of 3 mm. If the latter is reduced, the studied wave mode packet for the compared signals would match exactly at the peaks by both amplitude and time, and would no longer change. Thus, it is computationally optimal to use this size.

To optimize the study and its computation time, the choice of the best solver for the current time dependant

model is crucial. Multifrontal massively parallel sparse direct solver (MUMPS) is the default solver in COMSOL for the current physics used. Many users advise to use the parallel direct solver (PARDISO) for this kind of application. Both softwares solve large systems of linear equations on multicore processors thus distributing the allocated memory.<sup>50</sup> Another important factor to consider is the time step method used. Generalized alpha is the default transient stepping method in COMSOL. Backward differentiation formula (BDF) is another implicit time stepping method used. The latter is more stable and can be used for several purposes compared to the generalized alpha method, but concurrently generates more damping.<sup>51</sup> BDF is more robust and accurate for large step sizes used because it tends to smooth out any sharp gradients in the solution. This is not always desirable especially if the time step size is small enough to give accurate solution by itself. A brief comparison is made to test each solver with each step method by solving for the established mesh and an arbitrary cure time for the study. The computation time is shown in Table 3 for each solver-time step method used. Since all four waves from each simulation produced the exact same signal, the combination that yields the shortest solving time is chosen to solve for the current study: PARDISO – Generalized alpha. Unchecking the “Bunch-Kauffman pivoting” matrix factorization option generates a lower final computation time of approximately 79 min per one cure data point.

Finally, a parametric sweep tab is included in the study to account for the changes during curing in all nine listed CFRP mechanical properties. This is done for each cycle separately. Since the 4 hr-soak and the 3 hr-soak cure cycles are respectively 450 min and 390 min long, and the data is segmented to simulate cure data points each 5 minutes, a total number of 91 simulations for the 4 hr-soak cycle and 79 simulations for the 3 hr-soak cycle are needed. The time-dependent study is solving for a signal propagation time of 300  $\mu$ s in each simulation, which is sufficient to receive the  $A_0$  mode in all the curing stages. The time step interval is

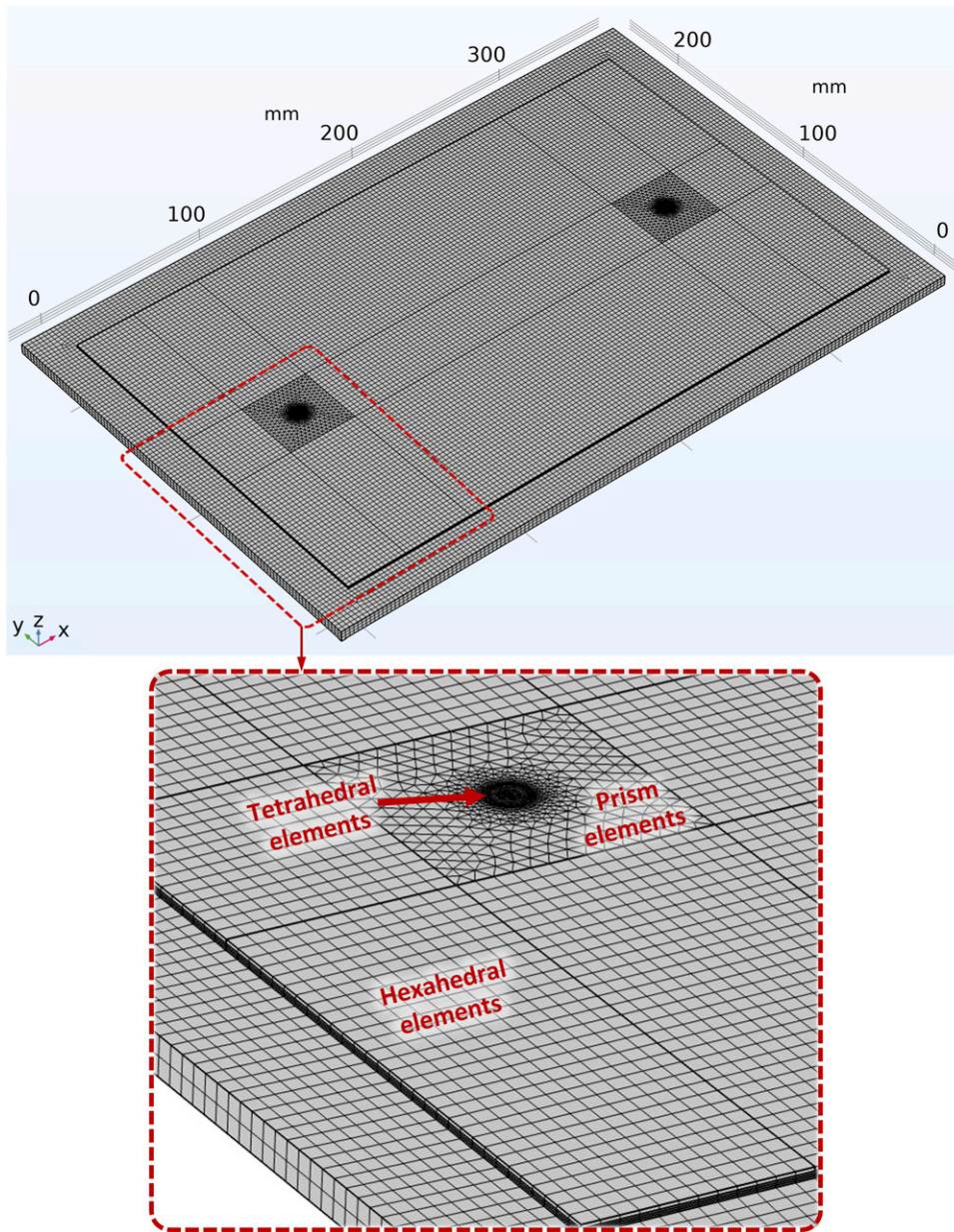


**Figure 8.** The fully meshed model with a maximum element size of 3 mm. There are 4443, 10,432, and 39,756 tetrahedrons, prisms, and hexahedrons, respectively present in the model, totaling at around  $55E + 3$  elements.

taken from experimental sampling and is  $0.42 \mu\text{s}$ . The importance of a parametric study is that the model runs only once for each cycle. All the data points are solved where each one data point simulation takes about 80 min, and the stored solutions are available for visualization and processing at the end of all simulations. Figure 9 shows a simple algorithm that summarizes the major steps taken before reaching valid numerical results from this computational model. This figure reviews all the previous numerical model discussions.

**Table 3.** Comparison between the computation time of each ‘solver - step method’ combination.

Solver - step method	Solving time
MUMPS – BDF	99 min 06 s
MUMPS - Generalized alpha	87 min 12 s
PARDISO – BDF	95 min 31 s
PARDISO - Generalized alpha	84 min 22 s

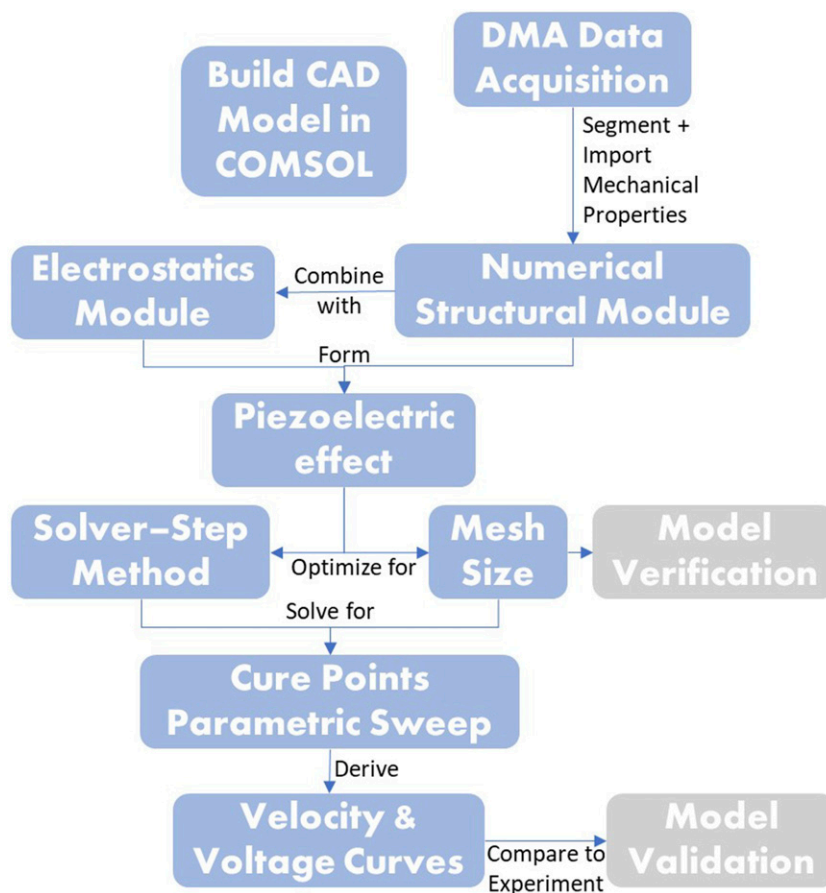


**Figure 9.** An algorithm showing the steps taken before and during solving the computational model.

## Results

At any spatial point inside the cylindrical volumes of the piezoelectric materials, the transmitted mechanical wave can be transformed back into an electrical signal that can be read in Volts. The signal is read at the center of the sensor PZT, meaning at the midpoint of the axis of the cylinder. This imitates the averaging of the signal from the whole PZT during experimental testing. First, we compare results for the fully cured CFRP with and without the inclusion of the PTFE film, as shown in the signals of Figure 10. The amplitude of the signal is clearly affected when adding the PTFE layer beneath the PZTs. This damping, although clearly visible, does not greatly distress the shape and speed of the first received wave mode packets. The boundary reflections, also shown in Figure 10, are of no interest in the current study. The obtained group velocity of the  $A_0$  mode is 2671 m/s without the PTFE and 2552 m/s with the PTFE. This is calculated by dividing the distance between the transducers (240 mm) by the time-of-flight between the actuator signal and the studied  $A_0$  mode wave packet. The

third peak of the wave packet is the one considered for time-of-flight calculations as it is the highest in the five-peak sinusoidal signal generated. From previous work, we know that the group velocity of the  $A_0$  mode in the aluminum tooling plate is 2735 m/s at 70 kHz which is very close to the speed of  $A_0$  mentioned in this case.<sup>4</sup> Since the wave is propagating inside both the CFRP and the aluminum tooling plate, the received signal is affected by their overlap and the velocity of the recorded  $A_0$  mode is thus altered. Knowing, from the woven CFRP dispersion curves in Figure 1, that the CFRP  $A_0$  group velocity at 70 kHz is around 1500 m/s, it is concluded that the wave modes are dominated by the tooling plate and the fluctuations inside the CFRP during curing vary the speeds accordingly.<sup>4</sup>

Figure 11 shows the comparison between experimental and numerical raw data points at two different cure times. Figure 11(a) compares the results for the 3 hr-soak cycle at 10 min which refers to the initiation of the first cure ramp (still at room temperature). The  $S_0$  mode is barely recorded in both signals and the electromagnetic noise, which mimics the actuated signal, is even replicated in a good manner due

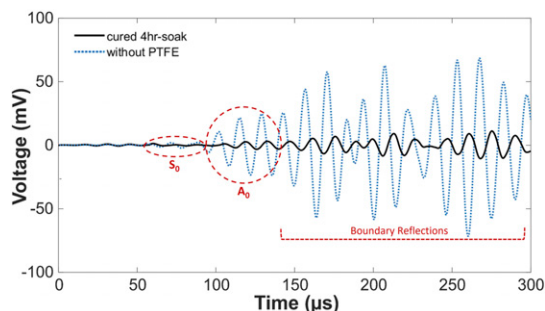


**Figure 10.** Computational signals for the fully cured state of the 4 hr-soak cycle with and without PTFE film.

to the accuracy of the dielectric constant of CFRP in the model. As for the studied  $A_0$  packet, all the peaks fit the experimental signal, so the group velocity is the same. The numerical signal is attenuated slightly more than its experimental counterpart, but the difference is minor. The second packet, where the reflections from the upper and lower aluminum plate boundaries assemble, deviates more from the experimental signal but is still distinguishable. Beyond this reflection, the experimental signal is very damped mainly because of the vacuum bagging tape seen in Figure 2. Thus, the numerical signal has higher peaks for the boundary reflections, but these packets are not of interest in our study. Figure 11(b) shows the last cure data point in the 4 h-soak cycle experimentally and numerically. The first received  $A_0$  packet also has the same group velocity as the peaks align but the experimental signal is more damped than the numerical one in this case, which makes more sense giving that the material attenuation is not accounted for in the computational model beyond the software's code. Despite this difference in attenuation, we can say that the numerical model gives good representation for the experiments, especially knowing all the simple mechanical assumptions taken in the model.

Signals obtained from the simulations of the 4 hr-soak and 3 hr-soak cycles are all analyzed by recording the group velocity from the third peak of the  $A_0$  mode and its voltage amplitude at that peak. The resultant group velocity and voltage curves versus FEA cure time are shown for both cycles in Figure 12. Compared to results of Figure 3, the same overall curve trends can be observed except for the clear decline in the voltage curves in Figure 12(b) after the ascent in the rubbery region, whereas in Figure 3(b) the voltage acts the same as the group velocity by increasing with a changed lower slope. This can be the effect of the assumptions made on Poisson's ratios during this curing period that are implemented inside the numerical model. To make sure that this is not the case, a brief sensitivity study is performed on the model where the Poisson's ratios are kept constant throughout the cure: the voltage analysis show the same diminishing factor

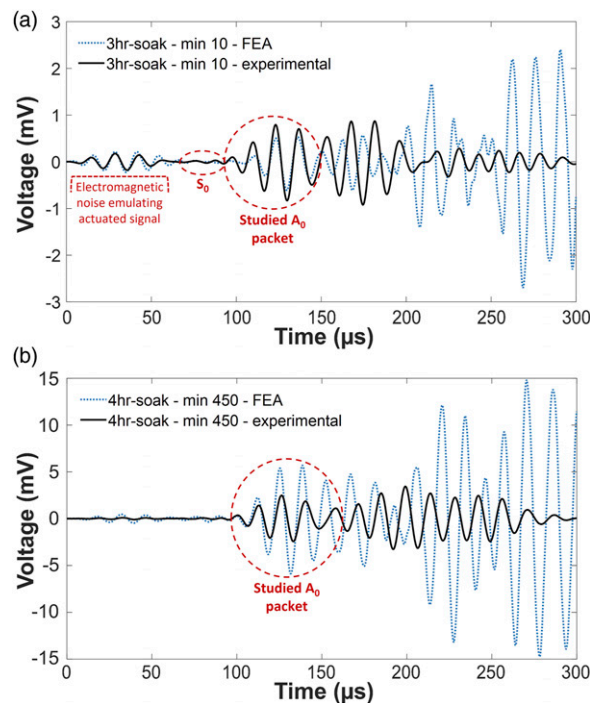


**Figure 11.** Comparing numerically computed signals from COMSOL to raw experimental data. (a) Shows the start of the 3hr-soak cure cycle, and (b) shows the end of the 4hr-soak cure cycle.

post-vitrification, thus, the numerical model is not highly dependent on this particular parameter. The minimum viscosity maxima sit at the same time numerically and experimentally for each cycle, which is at the end of the first soak. However, the gelation and vitrification points are shifted backwards in the numerical results and appear faster than in the experiments. This is expected since the mechanical properties in this model are imported from DMA results which have the same shift in these two cure parameters as discussed in the *Dynamic mechanical analysis* sub-section. However, when comparing the numerical results for the 3 hr-soak and 4 hr-soak cycles to each other, the parameters are still 60 min apart just like the cycle shortening outcome from the experimental analysis, proving that the numerical method operates effectively by monitoring a CFRP laminate during curing using minimal mechanical property knowledge. In the next section, the variation in gelation and vitrification timing between experimental and numerical results is scrutinized further.

## Discussion

### Lamb wavefields

One benefit from building a computational model for Lamb wave generation is to visualize the propagation of different modes within the structure. This gives further credibility to

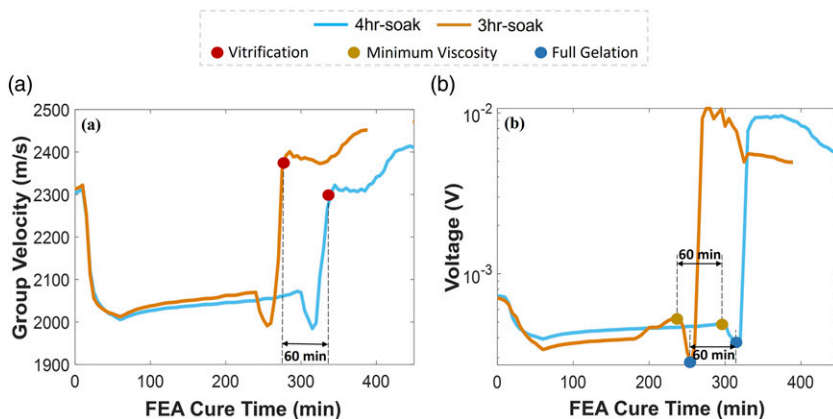


**Figure 12.** (a) Group velocity and (b) Amplitude of the first received  $A_0$  mode packet for both curing cycles extracted from the numerical model simulations.

many experimental statements such as identifying modes and is extremely helpful when dissecting the boundary and damage reflections. Since the wave generated inside the plates is mechanical, it is more desirable to see its speed as it gives better representation than the electric voltage. Different wave mode types propagate differently as discussed in the **Experimental testing** section. The symmetric  $S_0$  mode travels in-plane along with the propagation direction while the anti-symmetric  $A_0$  mode fluctuates in an out-of-plane manner as it propagates. Therefore, the anti-symmetric modes can be seen better from the velocity component in the  $z$ -direction ( $V_z$ ) as this is the out-of-plane through-thickness direction. The symmetric mode can be visualized better from either the  $x$ -direction ( $V_x$ ) or the  $y$ -direction ( $V_y$ ), but since the transducers are distant along the  $x$ -axis,  $V_x$  is used to scrutinize the  $S_0$  mode propagation. This does not mean that we can only find  $A_0$  along  $V_z$ , nor does it mean that we can only see  $S_0$  along  $V_x$ . In fact, both modes are included in all velocity components but  $A_0$  is more dominant along  $V_z$  while  $S_0$  is more clearly visible along  $V_x$  and  $V_y$ . In this study, since  $A_0$  is more dominant on this 70 kHz frequency for both CFRP (see Figure 1(a)) and aluminum,<sup>52</sup> it is also dominant over  $S_0$  in  $V_x$  component since the laid-up plates on top of one another make an easier path for  $A_0$  (out-of-plane) to travel across them while  $S_0$  (in-plane) is largely damped. In fact, one could argue that the setup of the experiment was always designed to suit the  $A_0$  mode and detect it clearly, rather than detecting a signal and analyzing its modes arbitrarily.

Figure 13 shows the propagating wave velocity profiles  $V_x$  (a) and  $V_z$  (b) in the PTFE-CFRP-Aluminum structure on both upper and lower sides and at different corresponding propagation times for the final curing point in the 4 h-soak cycle. This data point marks the examined signal of Figure 11(b) at 450 min. Figure 13 includes the mechanical properties of the CFRP at this cure point and the propagation time at the instant the snapshot is taken on top of the upper boundaries of parts (a) and (b). Figure 13(a) shows both

modes in the  $V_x$  component at an early time before reaching the sensor PZT on the right. Each mode is clearly distinguished by the different wavelength size and speed. On the lower side of the tooling plate (Side II), the wave modes have the same velocities but are slightly attenuated compared to the upper side, which makes sense since the wave is actuated from a 1.25 mm height above the 6 mm-thick aluminum plate. Figure 13(b) shows only the visible  $A_0$  mode from the  $V_z$  component at a time where the bulk of this mode hits the sensor PZT. The same figure also shows the boundary reflections generated by hitting the sides of the aluminum plate.

Figure 14 shows the propagating wave velocity profiles along the same directions and propagation times for the third curing point in the 3 hr-soak cycle. This data point marks the examined signal of Figure 11(a) at 10 min. On Side II for both Figure 14(a) and (b), we notice a similar behavior for the  $S_0$  and  $A_0$  modes as seen in Figure 13. On Side I, also the same behavior occurs for the travelling modes inside the PTFE-CFRP-Aluminum structure. However, an added wave packet with smaller wavelength than both modes is shown in the vicinity of the actuator PZT. This is clearly the effect caused by the decreased mechanical properties of the CFRP at the beginning of the cycle. This is why this mode is correlated with the composite laminate tested and not with the whole structure, especially since it does not show on Side II. Particularly, this can be the  $A_0$  mode generated inside the CFRP solely or inside the PTFE-CFRP structure. In our previous analysis, it was always assumed that the CFRP  $A_0$  mode was travelling inside the aluminum and creating a combined anti-symmetric mode that was analyzed throughout the cycle.<sup>4,5</sup> That mode would initially reflect on thickness boundaries of the aluminum plate and yield the  $S_0$  and  $A_0$  modes seen during the entirety of curing. Now, however, it is clear that this assumption was incorrect. The added CFRP  $A_0$  mode when the mechanical properties are lower show that the excited wave is initially a symmetric mode inside the CFRP that reflects near the

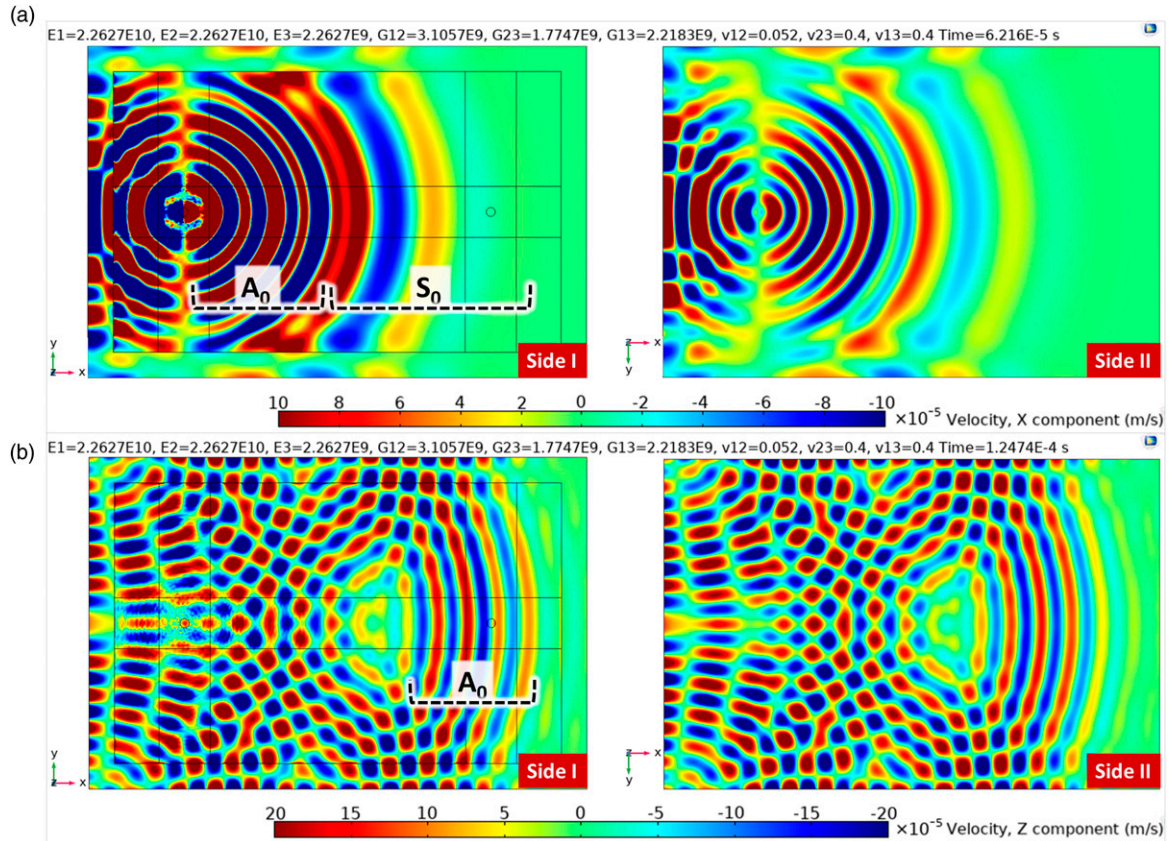


**Figure 13.** Upper and lower views of the Lamb waves velocity profiles inside the PTFE-CFRP-Aluminum structure at 450 min cure time for the 4 h-soak cycle along the (a) X velocity component, and (b) Z velocity component.

actuator PZT boundaries thus creating both mode conversion and transmission phenomena which yields  $S_{\text{CFRP-0}}A_0$  and  $S_{\text{CFRP-0}}S_0$  modes inside the entire structure, especially inside the aluminum tooling plate which dominates the wave propagation because of its thickness and high mechanical properties. In Figure 13, the CFRP  $A_0$  mode does not show because it is faster as a result of the higher laminate properties. Thus, it blends with the total signal because the difference in speeds between them is lower. In Figure 14, the same CFRP  $A_0$  mode is so slow that it is almost trapped (static) inside the shown region and keeps reflecting off the actuated PZT and CFRP boundaries (especially shown in Side I of Figure 14(b)). Note that in Figure 14(b) Side I, the propagation of this slow CFRP  $A_0$  mode is not circular like all the other propagating modes in the structure. It resembles a filleted square that has its corners along the propagation directions. This is because the woven CFRP is considered quasi-isotropic along the x and y directions, and thus have higher mechanical properties along these fibers, resulting in faster wave propagation. Also, note that the mesh is not optimized to represent the wave propagation of such slow mode, meaning that the shown CFRP  $A_0$  mode is not solved for correctly and can have a slightly different behavior had

the model been meshed accordingly. That, however, is too computationally expensive and irrelevant for the scope of this study. We are only interested in the generated symmetric and anti-symmetric modes in the entire structure and the latter's changes during the curing process. Nevertheless, the computational model here allows better understanding and analysis of the wave propagation process by visualizing and understanding the velocity profiles.

#### Added cure parameter

To improve the comparison between the experimental and numerical findings of the group velocity and voltage curves versus cure time, the results are shown together in Figure 15. The previously assigned vitrification points for the numerical results from Figure 12 are changed because it is noticed that the velocity curves (Figure 12(a)) indicate a change of slope near the end of cure with times very close to the experimental vitrification times for both cycles (which are indicated by the slope change in the ascent). Figure 15(c) shows the new assigned vitrification points for the numerical results at 315 min and 375 min for the 3 hr-soak and 4 hr-soak cycles, respectively. These values compare very

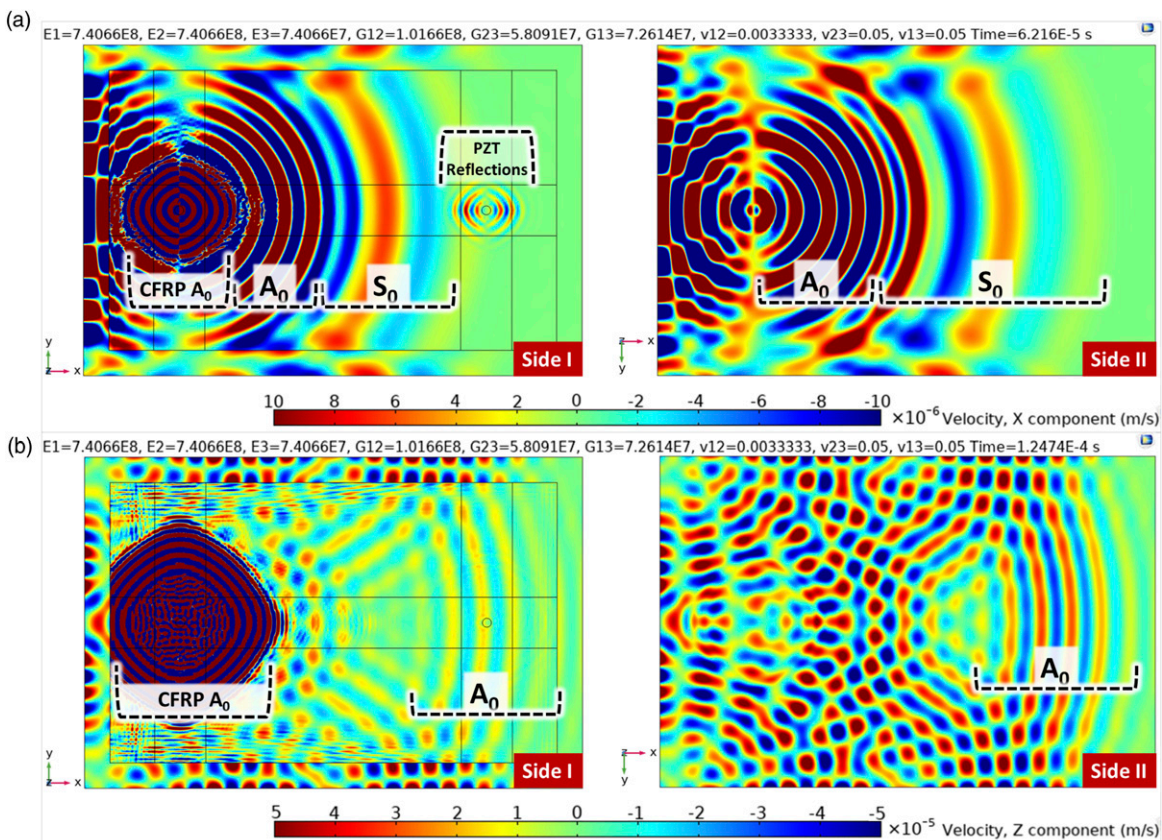


**Figure 14.** Upper and lower views of the Lamb waves velocity profiles inside the PTFE-CFRP-Aluminum structure at 10 min cure time for the 3 hr-soak cycle along the (a) X velocity component, and (b) Z velocity component.

closely to 305 min and 365 min vitrification points for the experimental 3 hr-soak and 4 hr-soak cycles. In Figure 12(a), they were assigned at 280 min and 340 min accordingly. The considered gelation points in Figure 12(b) are very close in time to the minimum viscosity points separated by only 15 min for each cycle. The new full gelation considerations in Figure 15(d) are at the end of the rubbery region ascent in the numerical voltage curves at 270 min and 330 min for the 3 hr-soak and 4 hr-soak cycles. Compared to the minima in experimental voltage curves of Figure 15(b), they differ by only 5 minutes since full gelation points are set to 275 min and 335 min for the 3 hr-soak and 4 hr-soak cycles in these experimental results. In Figure 12(b), they were assigned at 255 min and 315 min for the 3 hr-soak and 4 hr-soak cycles. The new times for full gelation and vitrification points for the numerical results (Figure 15(c) and (d)) make more sense than those assigned in Figure 12 since they are closer to their experimental counterparts (Figure 15(a) and (b)). If this is the correct case, there remain the minima of the numerical velocity and voltage curves in Figure 15(c) and (d) that is not assigned to neither full gelation nor vitrification. Since

this new parameter appears at the same time in the voltage and velocity curves for each cycle, it is labeled by a hollow black circle in both figures. The times here are 255 min and 315 min for the 3 hr-soak and 4 hr-soak, respectively. When projected up to the experimental results in Figure 15(a) and (b), it is shown how the black circle lies between the minimum viscosity and the full gelation points, in the second descent of the curves occurring during the second temperature ramp. Since this new parameter is fairly close to the minimum viscosity points, it can be implied that the initiation of the gelation process occurs at these times. Thus, a new added cure parameter called “gelation initiation” is assigned in Figure 15. This cure parameter is also shifted by exactly 60 min backwards for the 3 hr-soak cycle. If these assumptions are not correct, the differences between gelation and vitrification points for the ultrasonic experimental test and the DMA generated  $E'$  curves would still be due to the several reasons stated previously: difference in vacuum and bagging material, tooling plate and heat transfer consideration, and the difference in the length-to-thickness ratio of the specimens for both experiments.

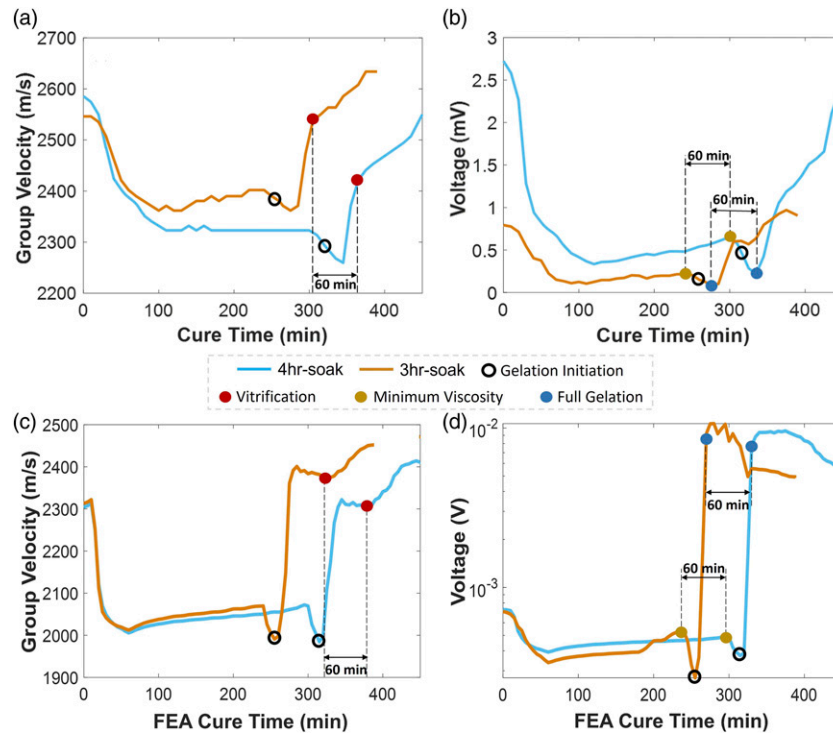


**Figure 15.** Rearrangement of the gelation and vitrification cure parameters after identifying the new ‘gelation initiation’ parameter. The figure shows (a) the experimental group velocity curves, (b) the experimental voltage curves, (c) the numerical group velocity curves, and (d) the numerical voltage curves, all versus cycle cure time.

Further studies and validation are needed to justify the inclusion of the new gelation initiation parameter and the rearrangement of full gelation and vitrification points for the numerical study. However, if accurate, these changes should also be applied to the DMA storage moduli curves since they have the main influence on the numerical model results considering all the CFRP material properties changes during the cure are extracted from these curves. Thus, the cure parameters in Figure 4 are rearranged accordingly to include the gelation initiation parameter and to shift the full gelation and vitrification parameters. Figure 16 shows the implementation of these changes and their effect on the adjusted rubbery and glassy states regions. The rubbery region now starts from the gelation initiation parameter, which is relatively close to the minimum viscosity, and extends to the new assumed vitrification time spot. The glassy state is also shifted to start from the latter cure parameter and extends to the end of the cure cycle.

### Study limitations

This is an effective numerical study that does not shy away from having multiple limitations due to all the assumptions made along the different sections. First, the DMA frequency range for the cure testing can be enlarged to get a more

accurate average  $E'$  curve. Also, the loss modulus  $E''$  and/or the  $\tan \delta$  parameter are not considered for this study. They could slightly change the implemented modulus curve in COMSOL if employed. The averaged storage moduli curves for both cycles are amplified by a factor of four for better signal propagation response in the software. On the other hand, the changes in moduli for CFRP are all based on the imported storage modulus changes. Aluminum and PTFE are assumed to have no property changes during the increase in temperature, whereas in reality, their mechanical properties have slight changes. Also, relative permittivity of the woven CFRP is assumed to stay constant during the cure, which is not entirely accurate. Modeling-wise, the exclusion of the different bagging consumables might affect the resulting signal. Particularly, modeling the vacuum gum tape correctly around the aluminum plate edges might improve the reflections accuracy of the studied mode. Additionally, viscoelasticity is ignored because it needs more experimental testing and generates large number of degrees of freedom and hefty computational time within the model. Further studies on the wavefield velocity profile are required to validate the claims about the slow CFRP  $A_0$  mode at uncured stages. Finally, theoretical and experimental validation is needed to justify the statements about the new “gelation initiation” cure parameter.

**Practical importance of the numerical model**

Since the crosslinking reaction is irreversible, the absolute values of voltage and velocity fluctuations can be integrated over time using the following equation<sup>53</sup>:

$$\int_{t_1}^{t_n} X dt \approx \sum_{i=1}^{n-2} (t_{i+1} - t_i) (|x_{i+2} - x_{i+1}| + |x_{i+1} - x_i|); \quad (5)$$

where  $x_i$  is the studied parameter (voltage or velocity) at a time  $t_i$ . The data is then normalized to get the progress of reaction (POR) curves, or degree of cure, of experimental and numerical results for each parameter and for each curing cycle. The results are shown in Figure 17(a) and (b) for the POR curves integrated from velocity and voltage curves, respectively. The figures compare POR from experimental

and numerical studies at both cycles. The velocity POR curves show very similar trends between the numerical and experimental trends for each cycle. The FEA curves have a slight lead in time after the gelation process commences. This is understandable since the DMA curing parameters occur prior to those of the ultrasonically tested experiments. Other than that, the numerical trends compare to their experimental counterparts quite effectively. The FEA voltage POR curves, however, have very low values compared to the experimental voltage POR curves, until minimum viscosity occurs. The curves then match for both cycles until the end of the cure.

This preliminary calculation of the degree of cure in the form of POR lays the roadmap for future projects that expand on the use of this numerical model. The end goal is to reach a full digital twin that conveys information to the

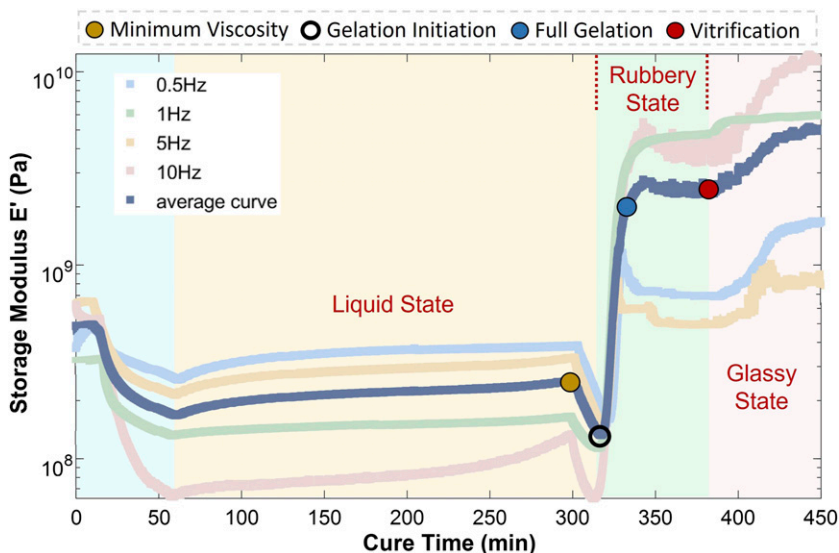


**Figure 16.** Rearranged rubbery and glassy states for the DMA 4 hr-soak curing results of the woven CFRP specimens tested with different frequencies. The rearrangement includes the new assumed “gelation initiation” cure parameter where the rubbery region starts. The relocated vitrification point also shifts the rubbery region end/glassy region start.

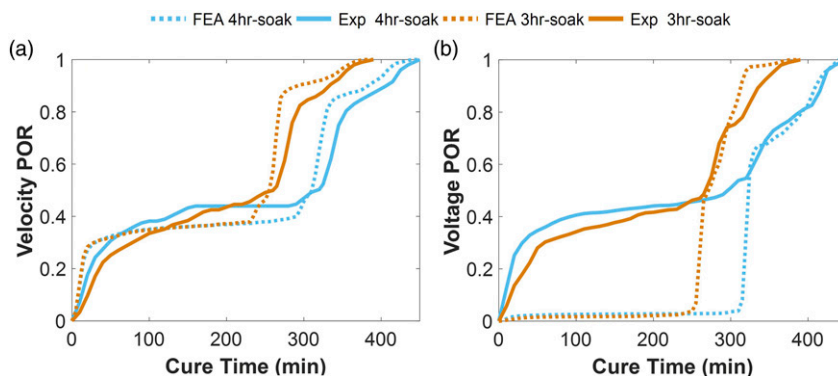


**Figure 17.** Progress of reaction (POR) curves normalized versus cure time as derived from (a) group velocity curves and (b) voltage curves. These results are shown for both cycles experimentally and numerically.

user prior to the experimental setup, thus, optimizing the entire cure monitoring process and reducing material waste. Reaching this stage would require, as previously mentioned, the addition of other modules to the numerical model. These are ‘heat transfer’ and ‘differential equations’ modules to emulate the chemical reaction effect by simulating the curing kinetics. This addition needs prior DSC testing to acquire all the kinetic constants for the Arrhenius equation of the curing CFRP. Viscoelastic sub-module would also be required to simulate the proper mechanical performance of the curing polymer composite. Supplementing the numerical model with the latter module demands stress-relaxation experiments to find all the constants during several curing phases. Combining all of these additions with the current developed model will definitely add value and novelty in future advancements. The numerical model would then be used to simulate new parts and structures that have different shapes and sizes where the cure monitoring readings would behave distinctly for each part. The numerical cure monitoring of complex shapes prior to fabrication gives the objective of this work a real practical importance, especially that the ultrasonic guided waves technique is valid for systems that cure at any pace, whether slow or rapid.

## Conclusion

In this work, a numerical model for cure monitoring of a shortened cycle CFRP laminate using guided Lamb waves is presented. First, Lamb waves fundamentals are explained, and the experimental ultrasonic results and conclusions are described such that the three main cure parameters: minimum viscosity, gelation, and vitrification are introduced on the velocity and voltage curves. Then, DMA curing storage modulus results are extracted for both the original and a trimmed cycle by 1 hour and imported into COMSOL Multiphysics after segmenting data points each 5 min and amplifying the curve trends by a constant factor. All CFRP mechanical properties are taken as function of the  $E'$  trend, each with respect to their known final cured stage value. The numerical model is introduced by combining the solid mechanics and electrostatics physics in COMSOL. The geometry and mesh are described and the criteria for the time-dependent solver is defined. The numerical results show that the Lamb wave received signals match the experimental raw data especially in the studied region of the first received anti-symmetric mode. The concluded velocity and voltage curves are then compared to the experimental results as the cure parameters are shown clearly but deviate because of the DMA  $E'$  curve trends. Then, velocity profiles of the Lamb wave-fields in the  $x$  and  $z$  directions are scrutinized. Additionally, a new cure parameter called “gelation initiation” is proposed by analyzing the numerically generated

voltage and velocity curves versus cure time results. Finally, degree of cure is integrated for both cure cycles from the velocity and voltage curves and compared numerically and experimentally. This model is a computational foundation to monitor the curing of several composites in the future. The cycle shortening is a major benefit to the industry and can be studied and applied on multiple composites with different cycles. More investigations are needed to improve the model and overcome some of the listed limitations present in the study.

## Acknowledgements

Recognition and gratitude are addressed to the University Research Board at the American University of Beirut and the Lebanese National Council for Scientific Research (CNRS).

## Author contributions

*EM*: Conceptualization, Formal analysis, Investigation, Validation, Writing - Original & Final Drafts, Visualization. *MH*: Conceptualization, Formal analysis, Supervision, Writing - Review and Editing, Funding acquisition.

## Declaration of conflicting interests

The author(s) declared no potential conflicts of interest with respect to the research, authorship, and/or publication of this article.

## Funding

The author(s) disclosed receipt of the following financial support for the research, authorship, and/or publication of this article: This work is supported by the University Research Board (URB) at the American University of Beirut grant number 103371.

## Research data statement

The authors confirm that most data supporting the findings of this study are available within the article and its supplementary materials. If needed, more data can be available from the corresponding author, *EM*, upon reasonable request.

## ORCID iD

Elie Mahfoud  <https://orcid.org/0000-0001-8239-4872>

## References

1. Koumoulos EP, Trompeta AF, Santos RM, et al. Research and development in carbon fibers and advanced high-performance composites supply chain in Europe: a roadmap for challenges and the industrial uptake. *J Compos Sci* 2019; 3(3): 86.
2. Oromiehie E, Garbe U and Gangadhara Prusty B. Porosity analysis of carbon fibre-reinforced polymer laminates manufactured using automated fibre placement. *J Compos Mater*

- 2019; 54(9): 1217–1231.
3. Van Grootel A, Chang J, Wardle BL, et al. Manufacturing variability drives significant environmental and economic impact: the case of carbon fiber reinforced polymer composites in the aerospace industry. *J Clean Prod* 2020; 261: 121087.
  4. Mahfoud E and Harb M. Reusable Piezo-sandwiched PTFE film for in-process monitoring of advanced composites. *J Intell Mater Syst Struct* 2021; 32(20): 2463–2476.
  5. Mahfoud E and Harb M. Assessment of cure cycle shortening for advanced composites via ultrasonics and dynamic mechanical analysis. *J Reinf Plast Comp* 2022; 41: 073168442110591.
  6. Michel M and Ferrier E. Effect of curing temperature conditions on glass transition temperature values of epoxy polymer used for wet lay-up applications. *Constr Build Mater* 2020; 231: 117206.
  7. Pang KP and Gillham JK. Competition between cure and thermal degradation in a high TG epoxy system: effect of time and temperature of isothermal cure on the glass transition temperature. *J Appl Polym Sci* 1990; 39(4): 909–933.
  8. Braun U, Balabanovich AI, Schartel B, et al. Influence of the oxidation state of phosphorus on the decomposition and fire behaviour of flame-retarded epoxy resin composites. *Polymer* 2006; 47(26): 8495–8508.
  9. Sawicz-Kryniger K, Niezgoda P, Stalmach P, et al. Performance of FPT, FTIR and DSC methods in cure monitoring of epoxy resins. *Eur Polym J* 2022; 162: 110933.
  10. Kister G and Dossi E. Cure monitoring of CFRP composites by dynamic mechanical analyser. *Polym Test* 2015; 47: 71–78.
  11. Bilyeu B, Brostow W and Menard KP. Evaluation of the curing process in a fiber-reinforced epoxy composite by temperature-modulated and step scan DSC and DMA. *Mater Char Dyn Modulated Therm Anal Techn* 2001; 1: 49–63.
  12. Kahali Moghaddam M, Breede A, Chaloupka A, et al. Design, fabrication and embedding of microscale interdigital sensors for real-time cure monitoring during composite manufacturing. *Sens Actuators A Phys* 2016; 243: 123–133.
  13. Roberts SSJ and Davidson R. Cure and fabrication monitoring of composite materials with fibre-optic sensors. *Compos Sci Technol* 1993; 49(3): 265–276.
  14. Wang D, Yu G, Liu S, et al. Monitoring the setting process of cementitious materials using guided waves in thin rods. *Materials* 2021; 14(3): 566.
  15. Nawab Y, Casari P, Boyard N, et al. Characterization of the cure shrinkage, reaction kinetics, bulk modulus and thermal conductivity of thermoset resin from a single experiment. *J Mater Sci* 2012; 48(6): 2394–2403.
  16. Lindrose AM. Ultrasonic wave and moduli changes in a curing epoxy resin. *Exp Mech* 1978; 18(6): 227–232.
  17. Aggelis DG and Paipetis AS. Monitoring of resin curing and hardening by ultrasound. *Constr Build Mater* 2012; 26(1): 755–760.
  18. Maffezzoli A, Quarta E, Luprano VAM, et al. Cure monitoring of epoxy matrices for composites by ultrasonic wave propagation. *J Appl Polym Sci* 1999; 73(10): 1969–1977.
  19. Pavlopoulou S, Soutis C and Staszewski WJ. Cure monitoring through time–frequency analysis of guided ultrasonic waves. *Plastics Rubber and Composites* 2012; 41(4–5): 180–186.
  20. Lionetto F and Maffezzoli A. Monitoring the cure state of thermosetting resins by ultrasound. *Materials* 2013; 6(9): 3783–3804.
  21. Hudson TB and Yuan FG. Automated in-process cure monitoring of composite laminates using a guided wave-based system with high-temperature piezoelectric transducers. *J Nondestruct Eval Diagn Progn Eng Syst* 2018; 1(2): 021008.
  22. Aktas A, Krishnan L, Kandola B, et al. A cure modelling study of an unsaturated polyester resin system for the simulation of curing of fibre-reinforced composites during the vacuum infusion process. *J Compos Mater* 2014; 49(20): 2529–2540.
  23. Mizukami K, Ikeda T and Ogi K. Measurement of velocity and attenuation of ultrasonic guided wave for real-time estimation of cure-dependent anisotropic viscoelastic properties of carbon fiber-reinforced plastics. *Ultrasonics* 2019; 99: 105952.
  24. Anandan S, Dhaliwal GS, Huo Z, et al. Curing of thick thermoset composite laminates: multiphysics modeling and experiments. *Appl Compos Mater* 2017; 25(5): 1155–1168.
  25. Garschke C, Parlevliet PP, Weimer C, et al. Cure kinetics and viscosity modelling of a high-performance epoxy resin film. *Polym Test* 2013; 32(1): 150–157.
  26. Behzad T and Sain M. Finite element modeling of polymer curing in natural fiber reinforced composites. *Compos Sci Technol* 2007; 67(7–8): 1666–1673.
  27. Dai J, Xi S and Li D. Numerical analysis of curing residual stress and deformation in thermosetting composite laminates with comparison between different constitutive models. *Materials* 2019; 12(4): 572.
  28. Zheng Z and Zhang R. Implementation of a viscoelastic material model to simulate relaxation in glass transition. In: COMSOL Conference Proceedings. Boston, USA: September 16, 2014.
  29. Patham B. Multiphysics simulations of cure residual stresses and springback in a thermoset resin using a viscoelastic model with cure-temperature-time superposition. *J Appl Polym Sci* 2012; 129(3): 983–998.
  30. Yoo SH, Han MG, Hong JH, et al. Simulation of curing process of carbon/epoxy composite during autoclave degassing molding by considering phase changes of epoxy resin. *Compos B Eng* 2015; 77: 257–267.
  31. Kravchenko OG, Kravchenko SG, Casares A, et al. Digital image correlation measurement of resin chemical and thermal shrinkage after gelation. *J Mater Sci* 2015; 50(15): 5244–5252.

32. Liu L, Zhang BM, Wang DF, et al. Effects of cure cycles on void content and mechanical properties of composite laminates. *Compos Struct* 2006; 73(3): 303–309.
33. Pernice MF, De Carvalho NV, Ratcliffe JG, et al. Experimental study on delamination migration in composite laminates. *Compos A Appl Sc Manuf* 2015; 73: 20–34.
34. Lamb H. On waves in an elastic plate. *Proc R Soc Lon Ser A Math Phys Char* 1917; 93(648): 114–128.
35. Wang L and Yuan F. Group velocity and characteristic wave curves of lamb waves in composites: modeling and experiments. *Compos Sci Technol* 2007; 67(7–8): 1370–1384.
36. El Najjar J and Mustapha S. Condition assessment of timber utility poles using ultrasonic guided waves. *Constr Build Mater* 2021; 272: 121902.
37. Su Z, Ye L and Lu Y. Guided lamb waves for identification of damage in composite structures: a review. *J Sound Vib* 2006; 295(3–5): 753–780.
38. Harb MS and Yuan FG. Impact damage imaging using non-contact Act/LDV System. *Struct Health Monit* 2015; 15: 2567–2574.
39. Fakih MA, Tarraf J, Mustapha S, et al. Characterization of lamb waves propagation behavior in friction stir welded joints of dissimilar materials. In: Proceedings of the IWSHM. Stanford, CA, 12–14 September 2017, pp. 55–62.
40. Feng B, Ribeiro AL and Ramos HG. Interaction of lamb waves with the edges of a delamination in CFRP composites and a reference-free localization method for delamination. *Measurement* 2018; 122: 424–431.
41. Stark W. Investigation of the curing behaviour of carbon fibre epoxy prepreg by dynamic mechanical analysis DMA. *Polym Test* 2013; 32(2): 231–239.
42. Eddib AA and Chung DDL. Electric permittivity of carbon fiber. *Carbon* 2019; 143: 475–480.
43. Saseendran S, Wysocki M and Varna J. Evolution of viscoelastic behavior of a curing ly5052 epoxy resin in the glassy state. *Adv Manuf Polym Compos Sci* 2016; 2(2): 74–82.
44. O'Brien DJ, Sottos NR and White SR. Cure-dependent viscoelastic poisson's ratio of epoxy. *Exp Mech* 2007; 47(2): 237–249.
45. O'Brien DJ, Mather PT and White SR. Viscoelastic properties of an epoxy resin during cure. *J Compos Mater* 2001; 35(10): 883–904.
46. Grassia L and D'Amore A. The relative placement of linear viscoelastic functions in amorphous glassy polymers. *J Rheol (N Y N Y)* 2009; 53(2): 339–356.
47. Pang KP and Gillham JK. Anomalous behavior of cured epoxy resins: density at room temperature versus time and temperature of cure. *J Appl Polym Sci* 1989; 37(7): 1969–1991.
48. Moosburger-Will J, Greisel M and Horn S. Physical aging of partially crosslinked RTM6 epoxy resin. *J Appl Polym Sci* 2014; 131(23): 41121.
49. Ghose B, Balasubramaniam K, Krishnamurthy CV, et al. Two dimensional FEM simulation of ultrasonic wave propagation in isotropic Solid Media using COMSOL. In: COMSOL Conference Proceedings. Bengaluru, India, December 10 2010.
50. Schenk O and Gärtner K. Solving unsymmetric sparse systems of linear equations with Pardiso. *Future Gen Comp Syst* 2004; 20(3): 475–487.
51. Brugnano L and Magherini C. Blended general linear methods based on generalized BDF. In: AIP Conference Proceeding 2008.
52. Malaeb RA, Mahfoud EN and Harb MS. Decomposition of fundamental Lamb wave modes in complex metal structures using COMSOL®. In: COMSOL Conference Proceedings, Lausanne, Switzerland, 23 October 2018.
53. Liu X, Yu Y, Lomov SV, et al. The numerical and experimental investigations for the curing monitoring of woven composites with lamb waves. *Measurement* 2022; 200: 111604.